Pure Appl. Chem., Vol. 74, No. 9, pp. 1553–1570, 2002.
© 2002 IUPAC

Morphology of nanostructured materials*

M. K. Sanyal‡, A. Datta, and S. Hazra

Surface Physics Division, Saha Institute of Nuclear Physics, 1/AF Bidhannagar, Kolkata 700064, India

Abstract: Here we shall discuss the importance of grazing incidence X-ray scattering techniques in studying morphology of nanostructured materials confined in thin films and multilayers. In these studies, the shapes, sizes, and structures of nanostructured materials and their distribution in composites are investigated. These studies are important for understanding properties that may deviate considerably from the known bulk properties. We shall first outline basics of three X-ray scattering techniques, namely X-ray reflectivity, grazing incidence small-angle X-ray scattering, and grazing incidence diffraction, used for these studies. We shall then demonstrate the utility of these techniques using some known results.

INTRODUCTION

Morphology, that is, the study of form comprising shape, size, and structure, is important for materials research in general. For nanostructured materials, popularly known as nanomaterials, morphology has special significance since form, in this case, dictates physical and chemical properties [1,2]. Unlike bulk materials, properties of nanomaterials are strongly correlated to shape. This shape is attained during growth through a self-assembling process dictated by the interplay of size and molecular interactions [2,3]. Deviations from bulk properties become prominent as the size of nanomaterials starts to be comparable to the size of constituent molecules or to some other characteristic length scale like electron mean-free path [1]. In a typical application, one deals with a collection of nanomaterials, which may be dispersed in a matrix [4] forming a composite material. Properties of this nanocomposite are controlled not only by morphology of individual nanomaterials, but also by the nature of interactions, which, in turn, is determined by the distribution of the nanomaterials in the matrix [5]. In this article, we shall discuss the role of X-ray scattering techniques in determining morphology of nanomaterials and their distribution in a nanocomposite. We shall restrict ourselves here to materials that have been grown in the form of thin films and mulilayers, which are important for various technological applications.

Thin films and multilayer structures may introduce a 1D confinement effect in addition to the confinement effect arising due to size of individual nanomaterials in these films [6]. For example, in a thin film, the presence of different nanomaterials such as nanodots (nanoparticles), nanowires, and nanosheets can introduce an additional 3D, 2D, and 1D confinement effect, respectively [1]. In a multilayer structure, apart from atomic arrangements of deposited materials, the presence of interfaces defines an additional 1D periodicity. The additional 1D potential and associated interfaces of a multilayer modify all physical properties of the deposited materials considerably, and the properties can be tuned by controlling the shape of the 1D potential [7]. Many multilayered structures with increasing complexities have been produced, and a multilayer structure embedded with nanomaterials is one such example [1,8].

Pure Appl. Chem.* **74, 1489–1783 (2002). An issue of reviews and research papers based on lectures presented at the 2nd IUPAC Workshop on Advanced Materials (WAM II), Bangalore, India, 13–16 February 2002, on the theme of nanostructured advanced materials.

‡Corresponding author

In semiconductors, the directional nature of chemical bonds causes formation of extremely high-quality epitaxial multilayers [9]. In metals, however, bonding is less directional, and it is more difficult to achieve comparable perfection. Nevertheless, advanced crystal growth methods such as molecular beam epitaxy (MBE) and low-pressure metal organic vapor phase epitaxy (MOVPE) have now made possible the sequential monolayer-by-monolayer deposition not only of semiconductors but also for metals and insulators, and practically any combinations thereof [10]. Compositionally modulated multilayers have found a wide interest both in basic research, as well as in some areas of electronic and optoelectronic devices and X-ray mirror structures [11], magnetic recording devices [12], hard surface coatings [13], etc. A recent experimental advance, namely, strained-layer epitaxy and oriented nanodots in multilayers [14], has enabled us to tailor the band-gap almost at will. The production of such artificially structured materials may be called "band-gap engineering". By employing suitable organic reagents, various 2D and 3D arrays of nanocrystals of semiconductors and metals (both magnetic and nonmagnetic) have been assembled, and the morphology of these nanocrystals can be controlled quite well. This self-assembled growth process [2] may provide a low-cost alternative route to form nanodevices, which are generally grown in MBE facilities. Here we shall discuss some nanostructures of metals where physical properties are strongly dependent on the morphology.

Multilayered organic and metal-organic films are being studied actively to form model systems for biophysical application and to understand the self-assembling mechanism observed in physics and biology [15]. One of the easiest ways to achieve such a film with good ordering in the direction of growth is the Langmuir–Blodgett (LB) technique [16,17]. The LB films are very convenient systems for studying [18,19] melting of 2D solids, which is expected to be a continuous transition as opposed to melting of conventional 3D solids. Nanometer-sized semiconductor particles that exhibit quantum confinement effect in band structure can be formed by exposing suitable LB films to reactive gases [20]. Here we shall discuss results of X-ray reflectivity and diffuse scattering studies to reveal the enigmatic growth mechanism and interesting properties of LB films.

In the following sections, we present outlines of the experimental methods, especially the grazing incidence X-ray scattering techniques, required to carry out morphological studies of nanostructured materials, and then discuss in brief some of the recent results on semiconductor, metallic, and organic films.

EXPERIMENTAL TECHNIQUES

Surface scientists have traditionally used experimental probes that have small penetration depth, such as electrons, to study the structure of atoms at surfaces and interfaces (which are invariably present with bulk atoms!) of thin films and multilayers. However, owing to strong interactions of electrons at the surface, multiple scattering takes place, and, as a result, quantitative structure determination using only electron diffraction becomes problematic. By using X-rays and neutrons in grazing incidence, the scattering can be made surface-sensitive, and these radiations are increasingly being used to probe the structure of surfaces and interfaces [21]. In any case, X-ray sources of high brightness are needed for gathering sufficient scattered intensity from interfaces, as the number of atoms is orders of magnitude smaller than that in the bulk. Structural studies of thin films and multilayers using grazing incidence X-ray scattering techniques are becoming a very prominent field of research [21–23] owing to the availability of intense rotating anode sources and synchrotron sources.

Scanning probe microscopy (SPM) is another class of techniques that is finding wide application in surface characterization of various materials. Real space surface images obtained from this technique provide information complementary to the statistically averaged reciprocal space information obtained from scattering techniques [22–24]. In this class of microscopic techniques, the most common feature is that a sharp tip, which acts as an appropriate probe, is scanned in a raster fashion over the material to be studied. Different types of force are experienced when the sharp tip comes close to the sample sur-

face. Different techniques evolved under this family utilizing such different types of force. In this family [25], atomic force microscopy (AFM) is widely used as it can practically probe any types of surfaces—from metallic to nonmetallic, from hard to soft ones. On the other hand, the scanning tunneling microscope (STM) operates by the mechanism of tunneling of electrons between a small metallic tip and a conducting surface. The vertical resolution is achieved by the exponential dependence of the tunneling current on the tip-to-surface separation. A typical variation in current is an order of magnitude for every angstrom separation.

Apart from X-ray scattering techniques, which are sensitive to both top surfaces and buried interfaces, we shall use results of SPM techniques here, although these techniques probe only the top surface of thin films and multilayers.

Grazing incidence X-ray scattering techniques

Three different measurements (shown in Fig. 1) are used here to obtain different information regarding the structure and morphology of these materials. These techniques are X-ray reflectivity (XRR), grazing incidence small-angle X-ray scattering (GISAXS) and grazing incidence diffraction (GID). In these studies, X-ray scattering intensities are measured as a function of the wave vector $\boldsymbol{k}(k_x,k_y,k_z)$, and to enhance the sensitivity of X-rays to thin films these measurements are carried out in grazing angles of incidence. For specular and off-specular reflectivity measurements, one collects scattered X-ray intensity using a detector placed after a tight slit as a function of $\boldsymbol{q}$ ($2\boldsymbol{k} = \boldsymbol{k}_{\text{final}} - \boldsymbol{k}_{\text{initial}}$) by keeping one of the component, say $q_y = 0$. In these measurements, a well-collimated monochromatized incident X-ray beam strikes at a grazing angle α (starting from few milliradians), and the scattered intensity is recorded in the plane of incidence at an angle β. In this geometry, the other two components of $\boldsymbol{q}$ become $q_z = (2\pi/\lambda)\ (\sin\beta + \sin\alpha)$ and $q_x = (2\pi/\lambda)\ (\cos\beta - \cos\alpha)$, where λ is the wavelength of the X-ray used. In the case of specular reflectivity experiments $\alpha = \beta = \theta$, so that $q_x = 0$ and $q_z = (4\pi/\lambda)(\sin\theta)$,

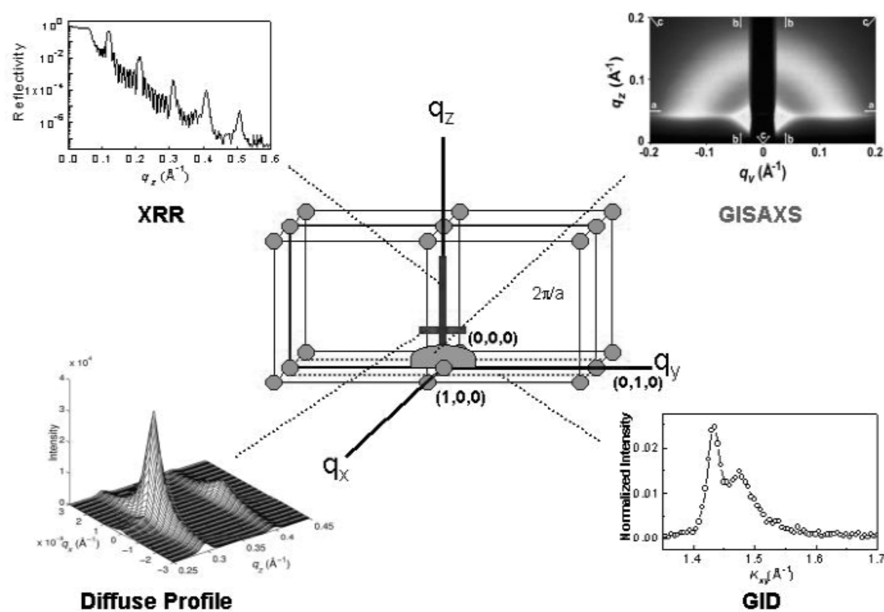

Fig. 1 Schematic of X-ray scattering techniques relating different types of scans to different regions of reciprocal space, with typical scan profiles.

and the scattering vector $\boldsymbol{q}$ is perpendicular to the surface, providing information about the mean electron density as a function of depth (z). For X-rays, wavelength refractive index n of any material is slightly less than 1. As a result, for any material we get a positive critical angle α_c and corresponding $q_c = 4\pi\sin\alpha_c/\lambda$ [22]. It should be noted here that at grazing incidence, the X-ray scattering is not generally sensitive to individual atoms and one can use continuous electron density profiles $\rho_{el}(\boldsymbol{r})$. Only in GID we approach large $\boldsymbol{q}$ with high in-plane angle (ϕ), and, as a result, we get in-plane diffraction peaks and $\rho_{el}(\boldsymbol{r})$ becomes discrete to exhibit atomic locations.

To have a better understanding of the correlation in an interface and between interfaces, we need a technique that is sensitive to in-plane morphology, and off-specular diffuse scattering directly provides us this information [23]. Generally, two types of diffuse data are collected to extract morphological information through height–height correlation at one interface and between interfaces in a multilayer. For transverse diffuse scattering measurements, the scattering angle $\alpha + \beta = 2\theta$ is maintained at a fixed value, while α and β are scanned. The longitudinal diffuse data are taken along the specular direction by keeping offset between α and β so that $q_x \neq 0$. The collected diffuse data are then plotted with proper normalization so that specular, transverse, and longitudinal data are all self-consistent.

In GID, one obtains in reciprocal space, rods of intensities, known as the crystal truncation rods (CTR), corresponding to a surface structure [26] instead of spots obtained for 3D structures. Once the intensity profiles of these rods are measured, methods of analysis for GID data are similar to that used in conventional X-ray crystallography measurements [27]. In these measurements, the X-ray beam is incident at a fixed angle α, just below the critical angle α_c of the film material, and the scattered intensity is measured as a function of β and in-plane angle (ϕ) between incidence and scattered X-ray beam. The CTR intensity profiles are collected using a linear position sensitive detector.

GISAXS measurements [28] are carried out at a fixed incidence angle, slightly greater than the critical angle α_c of the film, using a 2D detector fixed in y–z plane. In GISAXS measurements, the diffuse scattering intensity is collected over a very large area in reciprocal space. Here, illuminated area and the penetration depth, both of which depend on the chosen incidence angle, are kept constant, and the range of reciprocal space is controlled by varying sample to detector distance. This gives the possibility to measure very short correlation lengths (typically $\xi < 100$ Å), and, more importantly, the anisotropy of the scattering is determined. This is extremely useful in getting information about the way nanoparticles are distributed in thin films and multilayers.

We now discuss briefly the analysis techniques for extracting morphological information from these scattering measurements. The details of these techniques can be found in textbooks [29–33].

Specular and off-specular X-ray reflectivity

The scattering process in grazing incidence experiments is generally treated in Born approximation to extract the in-plane correlation at interfaces and the EDP as function of depth, from measured off-specular and specular reflectivity data, respectively. In Born approximation, measured intensity is related to the 3D Fourier transform of the electron density profile, as

$$I = I_0 \frac{r_0^2}{\sin\alpha} \left| \int d\boldsymbol{r} \rho_{el}(\boldsymbol{r}) \exp(-i\boldsymbol{q}.\boldsymbol{r}) \right|^2 \otimes \Re(\boldsymbol{q}) \tag{1}$$

where I_0 is the incident X-ray intensity and r_o is the scattering length (or classical radius) of electron. The second term in the above equation represents convolution with the resolution function (generally assumed to be Gaussian) of the measurement set-up. The $\sin\alpha$ in the denominator takes care of the projection of X-ray beam on the sample surface. For a simple surface of a material having electron density ρ, this equation can be written as [22]

$$I = I_0 \frac{2\pi\rho^2 r_0^2}{q_z^2 \sin\alpha} \int_0^\infty d\eta_{\|} \exp(-g(\eta_{\|}) q_z^2 / 2) \eta_{\|} J_0(q_{\|}\eta_{\|}) \otimes \Re(\boldsymbol{q}) \tag{2}$$

where $g(r_{||})$ [$= 2\sigma^2 - 2C(r_{||})$] is the height difference correlation function defined as $<[z(0) - z(r_{||})]^2>$, which is related to interfacial roughness parameter σ and height–height correlation function of a surface $C(r_{||}) \equiv <z(0)z(r_{||})>$. Generally, $C(r_{||})$ decays to zero as a function of in-plane lateral separation $r_{||}$, and in those cases, one can separate out the specular component from the diffuse component [22,23]. For example, in the case of single surface, the specular component becomes

$$R = \frac{I}{I_0} = \frac{16\pi^2\rho^2 r_0^2}{q_z^4}\exp(-q_z^2\sigma^2) \tag{3}$$

and the diffuse component becomes

$$I_d = I_0\frac{\rho^2 r_0^2}{q_z^2 \sin\alpha}\exp(-q_z^2\sigma^2)\int_0^\infty dr_{||}(\exp(-q_z^2 C(r_{||}))-1)r_{||}J_0(q_{||}r_{||}) \tag{4}$$

The formalism to obtain the scattering cross-section of X-rays for various surfaces with different types of morphology, characterized by different correlation functions $C(r_{||})$, have been discussed in detail elsewhere [3,7,22,23,29–31]. The specular component arises due to scattering from the average surface, while the diffuse or off-specular component comes from scattering by height fluctuations about this average surface. The specular component is directional, while the diffuse component is distributed around the specular direction. The type of interfacial height–height correlation decides the nature of the distribution of diffusely scattered photons around the specular direction and the ratio of the number of photons scattered in the specular to those in the diffuse directions. In general, for a given incident angle, an increase in the height fluctuation or roughness leads to an increase in the number of photons scattered into the diffuse channels at the expense of the photons scattered in the specular channel, keeping the sum total of the scattered photons the same [19].

It should be mentioned here that the reflectivity expression in Born approximation given above and the generalized expression for an arbitrary EDP $\rho(z)$ given by

$$R = R_F\left|\int dz\frac{d\rho(z)}{dz}\exp(-iq_z z)\right|^2 \tag{5}$$

fail to represent experimental data near critical angles. However, this formalism is very convenient for extending the calculation of specular and diffuse scattering to multilayer structures. It is generally observed that for any multilayer system, the morphology of the upper interface conforms to the lower one, and for these systems, expression of diffuse intensity given in eq. 4 can be used [22–24,29–31] for these conformal multilayers by replacing prefactor of the integral by $Rq_z/(2k\sin\alpha)$. Here, R is the generalized Born approximation reflectivity and R_F is the Fresnel reflectivity for a single surface given by

$$R_F = |r_{01}|^2 = \left|\frac{q_z - \sqrt{q_z^2 - q_c^2}}{q_z + \sqrt{q_z^2 - q_c^2}}\right|^2 \tag{6}$$

where r_{01} is reflectance between vacuum (0) and materials (1) with critical angle α_c. It should be mentioned here that for analyzing reflectivity profile, where data near critical angle is of prime importance, expression for reflectivity (R) obtained from exact calculation [29–31] should be used. For example, for a single film of thickness D, this expression becomes

$$R = \left|\frac{r_{01} + r_{12}\exp(i2q_z D)}{1 + r_{01}r_{12}\exp(i2q_z D)}\right|^2 \tag{7}$$

where $\boldsymbol{r}_{01}$ and $\boldsymbol{r}_{12}$ are the reflectances between vacuum/film and film/substrate, respectively. One can recover eq. 5 from eq. 7 by neglecting multiple scattering [29]. In eq. 7, we have assumed sharp interfaces, but for real multilayers one encounters a width in each interface that arises due to roughness and interdiffusions. Systematic diffuse scattering and reflectivity measurements are required to decipher these two convoluted information, as we shall discuss later.

Grazing incidence diffraction

In GID technique [21,26,27], we are generally interested in the scattering process where a total external reflection occurs at the interface, i.e., when incidence angle α is less than α_c, the critical angle, which is of the order of milliradians for X-rays.

Under this condition, the electric field decays to $1/e$ of its value at $z = 0$ within a depth of l below the interface given by

$$l \cong \frac{\lambda}{2\pi\sqrt{\alpha_c{}^2 - \alpha^2}} \tag{8}$$

assuming both α and α_c are small.

As for $\lambda \sim 1$ Å, α_c is proportional to λ, l is independent of λ at these incident angles. l ranges from 25 Å to 100 Å, inversely as the electron density of the medium. Thus, incident X-rays are confined within a depth of a few hundred Å below the interfacial plane, whereas they travel in the plane (x and y directions) with a wavelength close to the free-space wavelength. This is the condition for GID that is exploited to study the structure of the interfacial region at atomic resolution.

In the GID condition, the electron density should be written as superposition of charge clouds centered on atomic positions, as we start getting in-plane Bragg peaks here

$$\rho(\boldsymbol{r}) = \sum_n \sigma_n(\boldsymbol{r} - r_n) \tag{9}$$

Here, $\sigma_n(\xi)$ is the charge density within the atom at position $\boldsymbol{\xi}$ from the center of the nth atom, whereas $\boldsymbol{r}_n$ is the instantaneous position of the atom center. One can express the scattered intensity

$$I_s = \sum_n f_n(\boldsymbol{q}) \exp[-iq.r_n] \otimes \Re(\boldsymbol{q}) \tag{10}$$

Here, $f_n(\boldsymbol{q})$, the structure factor of the nth atom for the vector $\boldsymbol{q}$ can be written using eq. 1 as

$$f_n(\boldsymbol{q}) = \int \sigma_n(\xi) \exp[-i\boldsymbol{q}.\xi] d\xi \tag{11}$$

The general forms of components of the scattering vector are

$$\begin{gathered} \boldsymbol{q}_x \cong k_x - S_x, \boldsymbol{q}_y \cong k_y - S_y, \boldsymbol{q}_z = -i\tilde{k} - S_z, \text{with } \tilde{k} \equiv k\sqrt{\cos^2\alpha - \cos^2\alpha_c}, \\ \boldsymbol{S} = \text{incident wave vector} \end{gathered} \tag{12}$$

The imaginary part in $\boldsymbol{q}_z$ gives rise to a slow decay, and we can assume that $f_n(\boldsymbol{q})$ can be replaced by the ordinary atomic structure factors with $\boldsymbol{q} = (k_s - S_x, k_y - S_y, - S_z)$.

Grazing incidence small-angle X-ray scattering

As mentioned before, a combination of specular reflectivity and diffuse scattering has been extensively carried out to determine the structure of, especially, homogeneous monolayers and multilayered thin films [22,29–32]. Up to now, not much work has been done to study the morphology of heterogeneous thin films [28]. The study of a heterogeneous medium such as a surfactant dispersed in some solution has been carried out mostly through small-angle scattering (SAS) in transmission geometry to find out the shape, size, separation, and interaction of the surfactants in the solution [33]. Conventional SAS

technique cannot be used directly in the case of thin films owing to the presence of the substrate and the small amount of scattering material. This has recently been overcome by using GISAXS techniques. In this technique, the incoming beam impinges on the sample surface at an angle of incidence close to the critical angle for total external reflection, and the scattered intensity is measured in reflection geometry using a 2D detector. These measurements allow the determination of the off-specular scattering at fairly large angles. The anisotropy of the measured diffuse scattering provides us information regarding the shape and separation of the particles in the film.

For a heterogeneous thin film, where particles (clusters or pores) are randomly distributed in an amorphous matrix, the electron density can be written as [28]

$$\rho(\boldsymbol{r}) = \left[\rho_{\text{matrix}} + \Delta\rho \sum_i \delta(\boldsymbol{r} - \boldsymbol{r}_i) \otimes S_{\text{particle}}(\boldsymbol{r}_i) \right] S_F(\boldsymbol{r}) \tag{13}$$

where $\Delta\rho = \rho_{\text{particle}} - \rho_{\text{matrix}}$, $\delta(\boldsymbol{r} - \boldsymbol{r}_i)$ is related to the distribution of the particles, $S_{\text{particle}}(\boldsymbol{r}_i)$ is determined by the shape and size of the ith particle at a position r_i, and $S_F(\boldsymbol{r})$ is related to the finite dimension of the film. The total scattered intensity from a film can be calculated in the kinematical approximation using eq. 1.

We can assume that part of the incident beam is reflected by the film interfaces and part of it is scattered by particle (which have different electron densities compared to matrix) grains. Then, the total scattered intensity can be written as the sum of two intensities arising separately from the matrix and the particles (neglecting the matrix-particles cross-term) as

$$I(\boldsymbol{q}) = R(q_z) + I_{\text{particle}}(\boldsymbol{q}) \tag{14}$$

where $R(q_z)$ is the reflectivity part (discussed in details in the previous section) of the film considering uniform electron density. The $I_{\text{particle}}(\boldsymbol{q})$ is arising from particles and can be calculated considering size, shape, and distribution of the them in the matrix. If we consider spherical particles of radius R, distributed in the matrix according to a cumulative disorder with average separation d, then one can write [34]

$$I_{\text{particle}} \propto \frac{(\sin \boldsymbol{q}R - \boldsymbol{q}R\cos \boldsymbol{q}R)^2}{(\boldsymbol{q}R)^6} \times \frac{1 - \exp(-2\boldsymbol{q}^2\sigma_d^2)}{1 - 2\cos(\boldsymbol{q}d)\exp(-\boldsymbol{q}^2\sigma_d^2) + \exp(-2\boldsymbol{q}^2\sigma_d^2)} \tag{15}$$

where σ_d is the variance of d. In actual calculation, one has to consider the variance of R as well and take into account the effect of reduced dimension of the film.

CONFINED SYSTEMS

Metals and semiconductors

Metal films

The effect of confinement on electrical, magnetic, and optical properties of metals is a fascinating field of research. A metal cluster, confined from all three directions, may exhibit atom-like electronic states, giving rise to Coulomb-staircase features in current-voltage plots in place of a continuous straight line having a slope determined by the resistivity of the metal. One can expect to get variations in this Coulomb-staircase structure as the degree of confinement is varied [35]. Studies on metal films by SPM and X-ray reflectivity techniques can lead to an understanding of the effect of morphology on electrical transport properties. We have shown in Fig. 2 AFM and STM images of a typical Au film, sputter-deposited on Si(001), exhibiting the morphologies of these metal films. The reflectivity profile and corresponding EDP, which is proportional to the mass density profile of the deposited metal, are also shown. The results clearly indicate the formation of ellipsoidal islands. The morphology of these islands could be extracted from these complementary measurements [36]. STS measurements of these islands

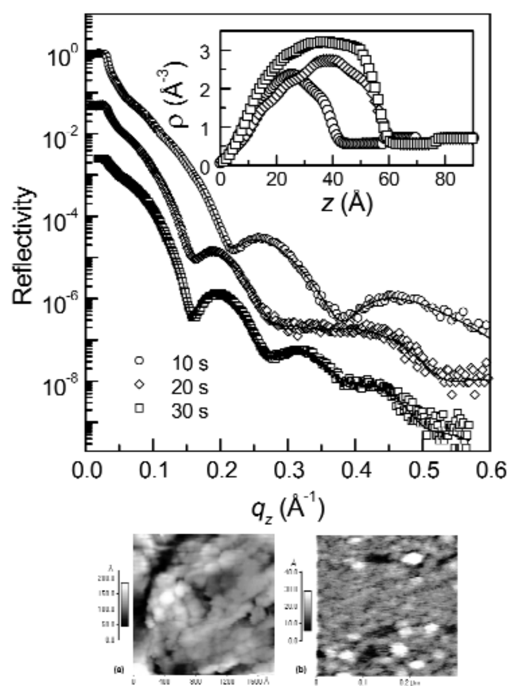

Fig. 2 Top panel: X-ray reflectivity and corresponding average EDP of Au films deposited on Si substrates for different durations of time. Bottom panel: Typical SPM images, STM (left) and AFM (right). Island growth of Au on Si substrate is evident.

having different density profiles show the opening of a "band-gap" in the Au clusters as cluster-size is reduced [37]. There is a possibility of forming quantum-well structures in metals by controlling this gap as a function of deposited thickness [38].

Extensive STM studies have been performed [39,40] to investigate the growth behavior of noble metals deposited on high-index Si(5512) surface and formation of nanowires. The periodicity (5.4 nm) of these nanowires matches that of the underlying Si surface. X-ray diffraction and diffuse scattering studies of epitaxial Ag films on Si(111) with and without embedded ferromagnetic metal (Co) nanocrystals have been performed to understand morphology of these films—important for magneto-resistive applications [41]. It should be noted that the so-called "phase problem" in X-ray scattering, which arises from the fact that one measures the scattered intensity and not the reflectance, could be overcome in case of confined systems [42,43]. In fact, it has been demonstrated now that one can reconstruct the shape of a nanocrystal by using a coherent X-ray source like a synchrotron [43].

Semiconductor multilayers

X-ray reflectivity curves of typical multilayered thin films are shown in Fig. 3 along with the obtained EDP. The interference (Kiessig) fringes [22] observed in the reflectivity curve are due to total film thickness. In the case of two-bilayer film, we get only the modulation in the fringes owing to the presence of bilayer period. However, in the case of nine-bilayer film, we get two types of modulations, Δq_K between two consecutive Kiessig fringes and Δq_B between two consecutive Bragg peaks. One can then calculate the total film thickness ($D_K = \pi/\Delta q_K$) and the bilayer separation ($D_B = \pi/\Delta q_B$). The presence of seven fringes between two Bragg peaks clearly shows that the film is formed by nine equal bilayers.

One needs to carry out detailed analysis of the reflectivity data to get accurate information regarding the thickness, interfacial widths, and electron densities of the individual layers in a multilayered thin

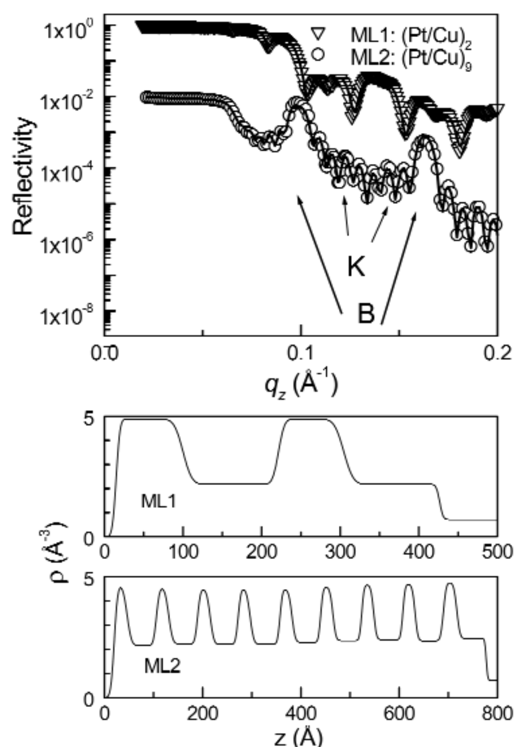

Fig. 3 Experimental (symbol) and fitted (lines) reflectivity curves of two Cu/Pt multilayer thin films on Si substrate. Corresponding EDPs are shown in the bottom two panels. Arrows marked by "B" and "K" in the reflectivity profiles correspond to the Bragg peaks and Keissig fringes, respectively.

film [22,29–31]. The x–y averaged EDP $\rho(z)$ of a multilayer is divided into slabs having constant electron densities as

$$\rho(z) = \sum_{1}^{n} \Delta\rho_i f(z_i, \sigma_i) \tag{16}$$

where $\Delta\rho_i$ is the change in electron density at ith interface located at a position z_i and f is an error function given by

$$f(z_i, \sigma_i) = f(z - z_i, \sigma_i) = \sigma_i^{-1}(2\pi)^{-1/2} \int_{-\infty}^{z-z_i} \exp(-t^2/2\sigma_i^2)dt \tag{17}$$

σ_i being the width of the ith interface. This EDP can then be used in eq. 5 to generate the reflectivity profile for fitting the experimental data [42]. One can also use the exact method [22,29–31] to calculate the reflectivity of the multilayer by modifying reflectance of ith interface as

$$r^i = r_F^i \exp\left(-\frac{q_z^2 \sigma_i^2}{2}\right) \tag{18}$$

The reflectivity of a multilayer, calculated using these reflectances for the interfaces, was then fitted to the experimental data using thickness, electron density (ρ), and interfacial width (σ_G) of each

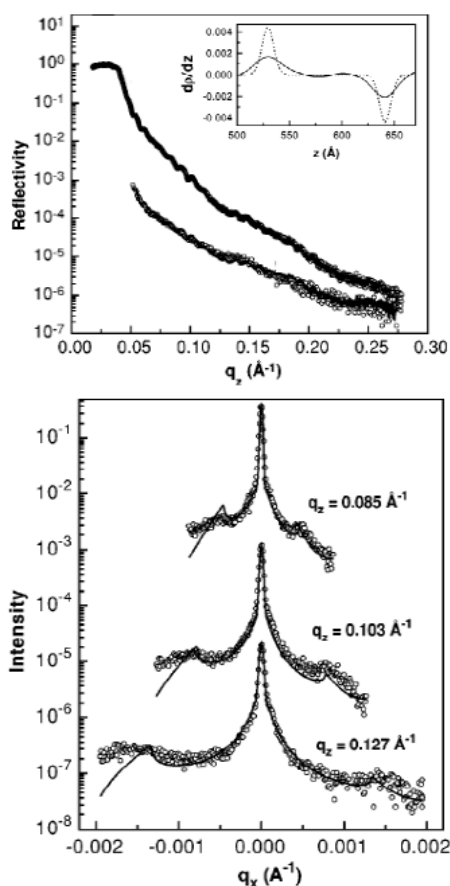

Fig. 4 Top panel: Specular reflectivity (top) and longitudinal off-specular reflectivity (bottom) for InP/InGaAs/InP quantum-well sample. Experimental data are shown by open circles and fitted curves by solid lines. Derivative of final EDP (solid line) and Gaussian function with $\sigma = 5.5$ Å (dotted line) corresponding to the conformal interfacial roughness in the quantum-well region are shown in the inset. Bottom panel: Transverse diffuse scattering intensity (open circles) as a function of q_x for three different values of q_z for a quantum-well sample are shown along with fit (solid line).

layer as fitting parameters. Best-fit curve thus obtained is shown in Fig. 3 along with EDP in the inset. The locations of different materials in the film are also indicated in the EDP. It should be mentioned here that this inversion process that is to extract real-space parameter from reflectivity data is a non-trivial exercise, and several schemes have been developed for this process [30,42–44]. It is known that interfacial width obtained from X-ray specular reflectivity study is actually a convolution of compositional and interfacial roughness profiles. On the other hand, diffuse scattering measurement provides us a measure of interfacial roughness profile. We shall present here the result of a diffuse scattering study of a conformal multilayer to illustrate this analysis technique.

In Fig. 4, we have shown the result of analysis of transverse diffuse data taken at three different q_z values for a quantum-well structure [42]. The height–height correlation function at lateral separation $r_{\|}$ between two conformal, self-affine, and rough interfaces is [23,42]

$$C(R) = \langle z(0)z(r_{\|})\rangle = \sigma^2 \exp\left[-\left(\frac{r_{\|}}{\xi}\right)^{2h}\right] \tag{19}$$

where σ, ξ, and h stand for roughness, in-plane correlation length, and roughness exponent, respectively [23]. These three parameters uniquely define the in-plane morphology of a surface/interface. It was observed that the expression of eq. 19 can represent a variety of surface/interface morphologies [29–31]. We obtained the values of σ, ξ, and h as 5.5 Å, 10 000 Å, and 0.45, respectively, by fitting the data with the above-mentioned analysis scheme. The same set of parameters was used to self-consistently calculate the longitudinal diffuse scattering profile (see Fig. 4). This profile follows the specular reflectivity profile closely, indicating conformality.

As the roughness here is conformal, one can take out the contribution of interfacial roughness from the interfacial width by deconvoluting the $\rho'(z)$, the derivative of obtained EDP from specular reflectivity data, with the roughness gaussian having $\sigma \sim 5.5$ Å, as obtained from fitting of diffuse scattering data. This deconvolution can be performed in Fourier space by utilizing the fact that the Fourier transform of the convolution of two functions is the product of the Fourier transforms of the functions. An interfacial profile (with variance of σ_G) observed in $\rho'(z)$ is shown in Fig. 4, along with the roughness Gaussian ($\sigma \sim 5.5$ Å), obtained from diffuse scattering analysis, at both the interfaces of the quantum well. The values of σ_G, found by fitting Gaussian functions, were 12 and 9 Å for the quantum-well interfaces with the cap layer and substrate, respectively [42]. This indicates that the interfacial widths are dominated by interdiffusion and substrate–quantum well interface is sharper than the quantum-well cap-layer interface. We have shown by systematic XRR and secondary emission mass spectroscopy (SIMS) measurements [45] that one can determine preferential interdiffusion profiles in semiconductor multilayer structures. Accurate determination of thickness, roughness, and interfacial width of multilayer structures is of prime importance for development of various devices based on quantum-well structures such as quantum cascade lasers, where frequency of emitted light can be tuned simply by tuning the thickness [11].

Langmuir–Blodgett films

Ordered multilayer films of organic and metal–organic complex materials can be deposited by a a relatively unsophisticated technique of repeated dipping of a solid substrate through a monomolecular layer (Langmuir monolayer) formed by spreading amphiphilic molecules on water surface. This is the Langmuir-Blodgett or LB technique. It is known that for depositing a LB film of a divalent fatty-acid-salt on a hydrophilic substrate, one needs to have water-to-air up-stroke first for attaching hydrophilic acid (head) group to the substrate with hydrocarbon chains (tails) pointing normal to the substrate. Then, a series of air-to-water-to-air stroke cycles are repeated to form a multilayered LB film well ordered in the direction of growth [16]. The schematic of a typical LB multilayer film, deposited on a hydrophilic substrate, is shown in Fig. 5. Also shown are the expected EDPs for an ideal film (dashed line) and a real LB film with propagating disorder (solid line). The role of molecular reorganization in the growth of LB films has been investigated with X-ray and neutron reflectivity techniques. The obtained density profiles are also shown in Fig. 5 along with experimental data and fits. Use of deuterated tails as markers directly shows that molecules get attached to the substrate in asymmetric configuration but, apart from the first layer, reorient themselves to a symmetric configuration. An exchange of molecules between first and second layers could also be detected [17].

X-ray studies have shown that the interfacial correlation of these films can vary from self-affine fractal [46], observed in diverse physical systems [47], to long-range logarithmic [20], characteristic of capillary waves on liquid surfaces [48]. Systematic studies of these interfacial morphologies [24] can provide us clear bases for the theoretical and simulation studies undertaken to link the evolution of interfacial morphology with possible growth mechanism of thin films [49–51]. Diffuse X-ray scattering from cadmium arachidate (CdA) films deposited on silicon and quartz exhibited peak shapes characteristic of self-affine and logarithmic interfacial correlation, respectively (Fig. 6), although the average vertical structure in these films was nearly identical as evident from the specular data [24]. The difference in the scaling of the widths and the specular to diffuse intensity ratio for the two profiles is

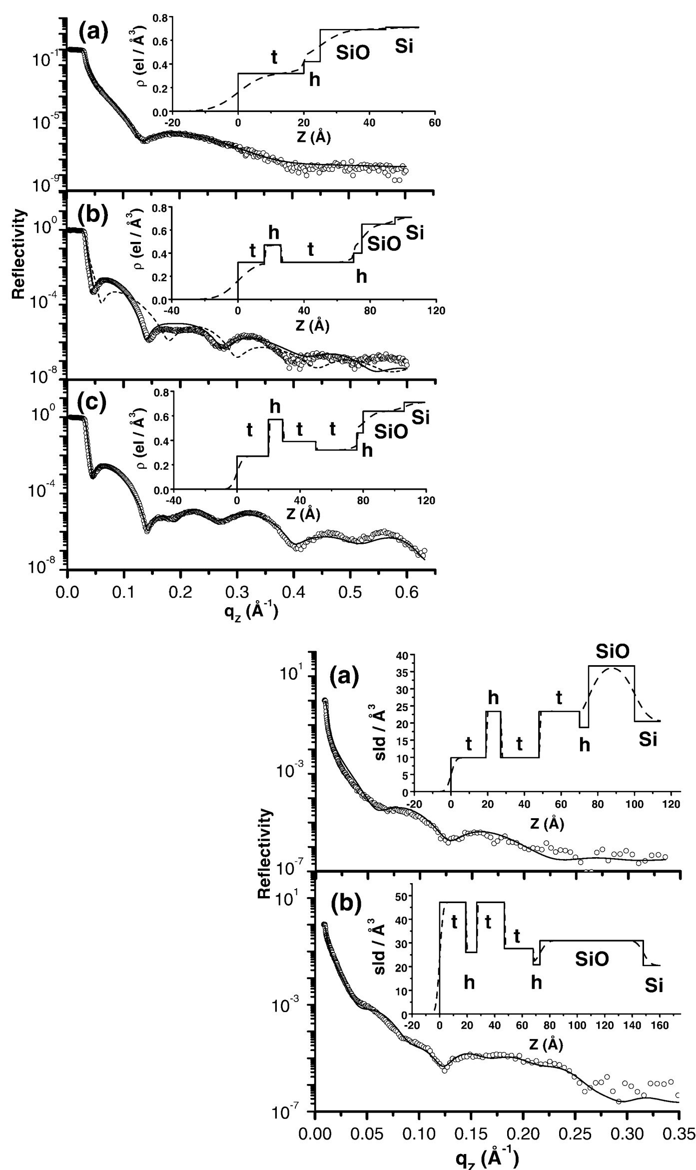

Fig. 5 Top panel: Experimental (symbols) and calculated (solid line) X-ray reflectivity profiles for (a) 1 ML, (b) 2 ML, and (c) 3 ML LB films of deuterated (D) and hydrogenated (H) cadmium stearate on Si(001). The respective electron density profiles with (dashed line) and without (solid line) roughness are shown in insets (t– tail; h–head). Bottom panel: Experimental (symbols) and calculated (solid line) neutron reflectivity profiles for (a) H-D-H and (b) D-H-D films on Si(001). The respective scattering length density ($\times 10^{-7}$) profiles are shown in insets. It is to be noted here that neutron scattering and electron density profiles used in the fitting come from the same material density profile. This approach improves the reliability of the obtained profile considerably.

clearly evident in the inset of Fig. 6. AFM studies on these LB films have provided additional information regarding the surface morphology. The roughness obtained from AFM measurements was plotted as a function of scan length for both films in Fig. 6. It can be readily observed that roughness of the film on silicon increased considerably with scan size to a certain cut-off length scale ~15 microns, and after that it saturated and the exponent was 0.5, as obtained from X-ray results. The variation of rough-

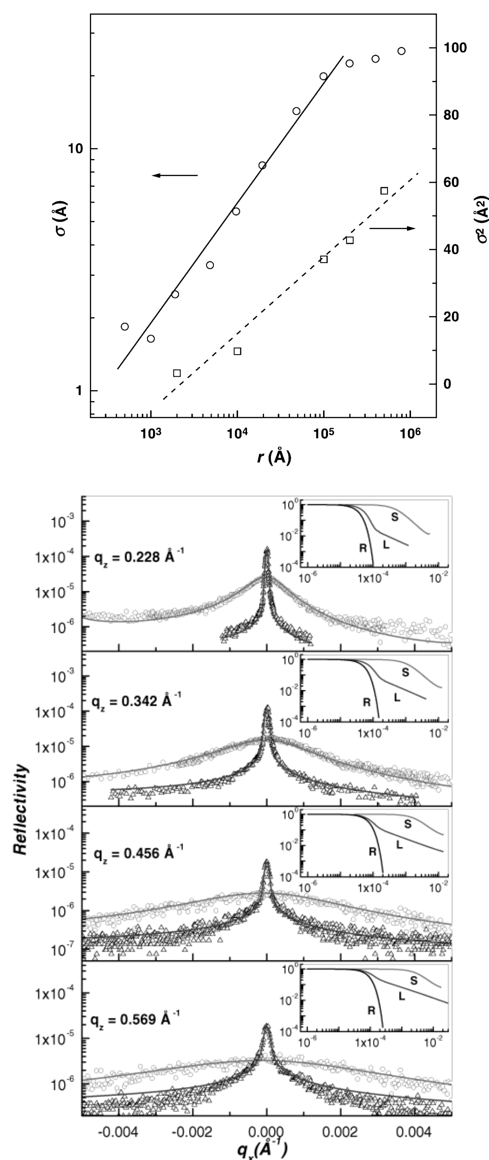

Fig. 6 Top panel: Variation of roughness (σ) with scan length CdA LB films. logσ vs. log r for the film on silicon (O). Solid line is the linear fit to the data below ξ ~ 15 µm. σ^2 vs. log r the film on quartz (□). Dashed line is the linear fit to data. Bottom panel: Transverse diffuse scattering data at four multilayer Bragg peak positions (indicated by the q_z values) for the LB films. The data for films on silicon (O) and quartz (Δ) are shown along with the calculated profiles (solid lines). In the insets, the functions F_S, F_L, and R (indicated by S, L, and R) are plotted against q_x in the log–log scale.

ness for the film on quartz was slow and followed a logarithmic relation, as observed in X-ray data. Based on these results, we have proposed [24] that the transfer of molecules from the Langmuir monolayer to a substrate takes place through 1D diffusion followed by 2D adsorption processes during formation of an LB film.

Several GID measurements have been performed to determine the structures of Langmuir monolayers, i.e., monolayers of amphiphilic molecules at the air–water interface and LB films [52]. The

Langmuir monolayers, the precursors of LB films, exhibit phase transitions with surface pressure, temperature, pH, and ion content of the water (subphase) [53]. Generally, when ions are present in the subphase, the monolayer becomes much better ordered and transfers more easily to a solid substrate in forming LB films [54]. The metal ions sometimes assemble into precise functional architectures in registry with the structure of the Langmuir monolayer [55], and Langmuir monolayers have been used as templates for the nucleation and growth of inorganic crystals of specific morphology and crystallographic orientation [56]. Theoretical calculations treat the organic film and ions as a 2D model of an electrochemical double layer and provide analytical expressions for the electrostatic potential and ion concentration at the surface [57]. As Langmuir monolayers are powders in the plane, the in-plane component of $\boldsymbol{q}$ (q_{xy}) cannot be decomposed further into *x* and *y* components. The total momentum transfer lies in a plane normal to the hydrocarbon chains, and an out-of-plane scan (q_z-scan) will yield a peak whose position provides the tilt of these chains while its width is inversely proportional to the thickness of the monolayer. Fig. 7 depicts the q_{xy}-scan of the monolayer at 10 ºC with subphase (having 10^{-5} M Pb^{2+} ions) pH ~5.5. Out-of-plane scans show a peak at $q_z = 0$, indicating that chains are untilted. The 2D lattice parameters can be obtained from the different q_{xy} peaks. GID has allowed the determination of the structures of inorganic–organic systems at the air–water interface and provided new insights into understanding template-directed nucleation phenomena [27,56–60].

Results of some recent experiments on LB films seem to match the earlier theoretical predictions on the melting of 2D crystals, which is expected to be continuous in nature and to proceed via an intermediate phase as compared to melting of isotropic 3D solids [18]. X-ray scattering and AFM studies on cadmium arachidate LB films have been carried out to understand the melting mechanism [19]. Diffuse scattering measurements at room temperature and at 110 ºC seem to indicate that the conformal interfacial correlation remains unchanged for two types of films shown in Fig. 6. The presence of strong

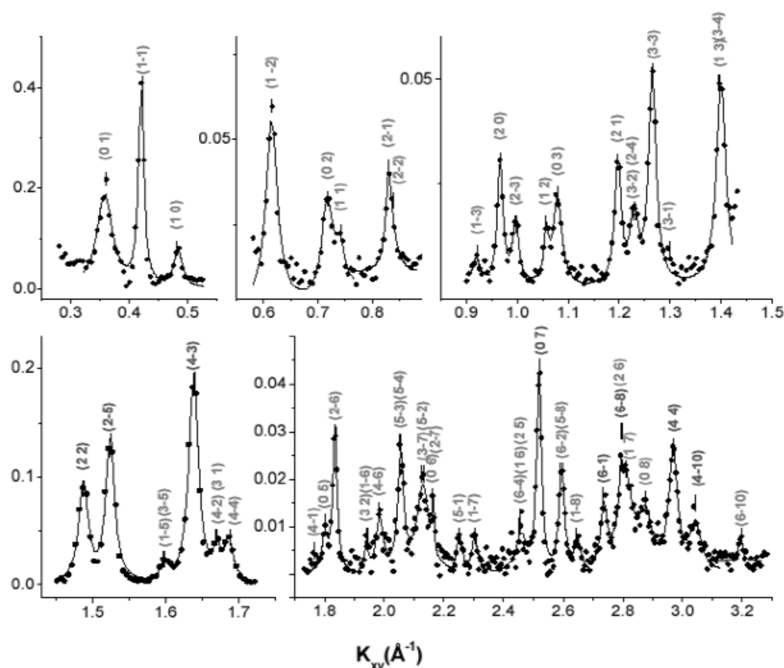

Fig. 7 Grazing incidence X-ray diffraction data from a heneicosanoic acid Langmuir monolayer with lead ions in the subphase. The lower-order peaks (2 2), (2 –5), and (4 –3), labeled in blue, correspond to the reciprocal lattice of the Langmuir monolayer (this identification is made from Bragg rod scans). The higher-order peaks (0 7), (6 –1), (6 –8), (4 4), (4 –10), labeled in blue, are also from the Langmuir monolayer. All other peaks are from the superlattice.

Kiessig fringes up to 85 ºC indicated that the film had more or less uniform thickness, and the presence of Bragg peaks shows that the LB bilayer remained intact. Beyond this temperature, the amplitude of the first observable Kiessig fringe started decreasing and vanished totally at 100 ºC. This might be an indication that the film thickness became inhomogeneous. At 110 ºC, the bilayer structure for both films broke down completely as is evident from the disappearance of the bilayer Bragg peaks. The general trend in melting seemed to be similar for both films. The close matching indicated that the mechanism of melting up to 100 ºC was independent of the type of interfacial correlation present in the untreated film. The trend of density reduction with temperature could either be due to vertical molecular interdiffusion or due to lateral expansion of the film. Since diffuse scattering measurements had ruled out significant vertical molecular interdiffusion, this trend of density reduction was a signature of lateral motion of molecules leading to expansion of the film, which has been confirmed by GID measurements.

Nanocomposite films

There are two major effects that govern physical properties of nanoclusters embedded in a film—the nature of the cluster–matrix interface and the intrinsic properties of the clusters. Synthesis of monodisperse clusters with well-defined surfaces remains a major goal in this field [2]. Recently, the growth of semiconducting nanoparticles in LB films has attracted much attention [22] primarily to exploit the highly ordered structure as a matrix to obtain better control over the size distribution, geometry, and stabilization of the particles. Ceramic metal (cermet) thin films constitute another variety of nanocomposite films of considerable interest as useful devices to absorb radiation in the visible and near infrared region of solar spectrum. The nanoparticles are formed by exposing preformed LB films, usually of the metal salt of long-chain carboxylic acids, to reactive gases. However the mechanisms of particle growth in the film, or the processes, which control the size of the particles formed in the film, are not well understood.

The formation of PbS particles was studied [61] by exposure of LB films of lead stearate to H_2S gas using X-ray diffraction and optical spectroscopy. The results indicated that the bilayer separation of the films after exposure was nearly the same as that of the unexposed lead stearate film, and the PbS particles formed remained confined with the cage of the carboxylic ion group of adjacent layer. It was suggested that PbS particles existed either in the form of 2D sheets or lines. Recent FTIR and X-ray diffraction measurements [62] by the same group on lead salts of amphiphilic oligomers (with variable carboxylic group to hydrocarbon chain ratio as compared to the 1:1 ratio in simple fatty acids) also indicated that PbS nanoparticles were formed without disturbing the layered structure of the unexposed films.

The formation of cadmium sulfide (CdS) nanoparticle in LB films has been investigated using X-ray scattering technique [20]. This can be done by looking at the LB interfaces before and after the formation of CdS nanoparticles. Specular reflectivity and diffuse scattering measurements of as-prepared and 60 min H_2S-exposed 9 ML LB films have been carried out to study the interfacial properties. The formation of CdS nanoparticles in the H_2S-exposed LB film was confirmed by UV–vis spectroscopy. It was found from reflectivity that the molecular stacking of LB structure was not disturbed due to H_2S exposure and the fact the CdS nanoparticles remained confined within the interfacial regions (of thickness 14 Å) around the metal sites (see Fig. 8).

Application of GISAXS technique to determine size, shape, and distribution of nanoparticles in thin films and multilayers is becoming important since conventional small-angle scattering experiments cannot be employed for such samples. Typical GISAXS image of a Pt–Al_2O_3 nanocermet thin film [28,45] collected using image plate is shown in Fig. 1. Half-annular ring observed is the characteristic of the separation of particles present in the film. For low concentration of particles, it is well known that the size of the particles can be estimated from the slope of the Guinier plot, similar to that done in conventional SAS analysis [33]. The particle size, shape, and distribution can be estimated fitting the

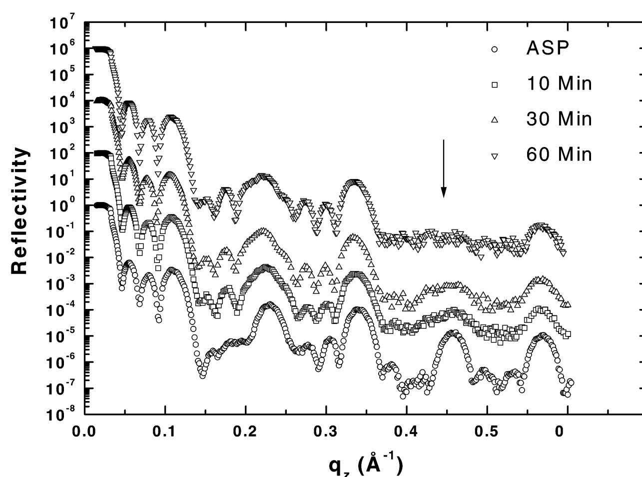

Fig. 8 Specular reflectivity data for 9 ML CdA LB film and films exposed to H_2S gas for different durations. Systematic decay of the fourth Bragg peak (indicated by the arrow) with increased time of exposure to H_2S is clearly evident. This extinction is arising due to formation of the CdS interfacial layer.

GISAXS image with the expression of I_{particle} given in eq. 15. The relevant parameters that are obtained from the fit are the radius R of the particles, the interparticle distance d, and the variance of these distributions. Any asymmetry in the shape or distribution of the particles can also be estimated from this analysis. GISAXS technique is found to be applicable in determination of size, shape, and distribution of nanomaterials in various composite films [63].

In this article, we have discussed the merit of X-ray scattering techniques in determining morphology of nanostructured materials. These studies are important to understand not only the growth mechanisms [17,20,24,28,36,42,45] of these materials but also the unusual properties of nanomaterials such as continuous melting process [19,64,65], negative thermal expansion [66], and semiconductor-like transport properties of metals [2,35,37,38].

REFERENCES

1. A. S. Edelstein and R. C. Cammarata (Eds.). *Nanomaterials: Synthesis, Properties and Applications*, IOP, Bristol (1998).
2. C. N. R. Rao and A. K. Cheetham. *J. Mater. Chem*. **11**, 2887 (2001).
3. Th. Zemb, M. Dubois, B. Deme, T. Gulik-Krzywicki. *Science* **283**, 816 (1999).
4. M. D. Hollingsworth. *Science* **295**, 2410 (2002).
5. M. Muthukumar, C. K. Ober, E. L. Thomas. *Science* **277**, 1225 (1997).
6. L. Esaki and L. L. Chang. *Phys. Rev. Lett*. **33**, 495 (1974).
7. E. E. Mende, L. L. Chang, G. Landgren, R. Ludeke, L. Esaki, F. H. Pollak. *Phys. Rev. Lett*. **46**, 1230 (1981).
8. O. Ikkala and G. ten Brinke. *Science* **295**, 2407 (2002).
9. C. Weissbuch and B. Vintner. *Quantum Semiconductor Structures: Fundamentals and Applications*, Academic, Boston (1991).
10. M. A. Hermann and D. Sitter. *Molecular Beam Epitaxy*, Springer, Berlin, (1998).
11. F. Capasso, C. Gmachl, D. L. Sivco, A. Y. Cho. *Phys. Today* **55**, 34 (2002).
12. F. J. Himpsel. *Adv. Phys*. **47**, 511 (1998).
13. T. Li, Q. Lou, J. Dong, Y. Wei, J. Liu. *App. Surf. Sci.* **172**, 331 (2001).
14. C. Teichert. *Phys. Rep.* **365**, 335 (2002).

15. A. Sellinger, P. M. Weiss, A. Nguyen, Y. Lu, R. A. Assink, W. Gong, C. Jeffrey Brinker. *Nature* **394**, 256 (1998).
16. G. L. Gaines. *Insoluble Monolayers at the Liquid–Gas Interface, Interscience*, New York (1966).
17. M. K. Sanyal, M. K. Mukhopadhyay, M. Mukherjee, A. Datta, J. K. Basu, J. Penfold. *Phys. Rev. B* **65**, 033409 (2002).
18. H. D. Sikes and D. K. Schwartz. *Science* **278**, 1604 (1997).
19. J. K. Basu, M. K. Sanyal, M. Mukherjee, S. Banerjee. *Phys. Rev. B* **62**, 11109 (2000).
20. J. K. Basu and M. K. Sanyal. *Phys. Rev. Lett*. **79**, 4617 (1997).
21. *Current Science*, Special Issue on Surface Characterization, M. K. Sanyal (Ed.) **78**, 1445–1531 (2000).
22. J. K. Basu and M. K. Sanyal. *Phys. Rep*. **363**, 1 (2002).
23. S. K. Sinha, E. B. Sirota, S. Garoff, H. B. Stanley. *Phys. Rev. B* **38**, 2297 (1988).
24. J. K. Basu, S. Hazra, M. K. Sanyal. *Phys. Rev. Lett.* **82**, 4675 (1999).
25. D. Sarid. *Scanning Force Microscopy*, Oxford University Press, New York (1991); C. J. Chen. *Introduction to Scanning Tunneling Microscopy*, Oxford University Press, New York, (1993).
26. I. K. Robinson and D. J. Tweet. *Rep. Prog. Phys*. **55**, 599 (1992).
27. J. Als-Nielsen D. Jacquemann, K. Kjaer, F. Leveiller, M. Lahav, L. Leseirowitz. *Phys. Rep.* **246**, 251 (1994).
28. S. Hazra, A. Gibaud, A. Desert, C. Sella, A. Naudon. *Physica B* **283**, 97 (2000).
29. J. Daillant and A. Gibaud (Eds.). *X-ray and Neutron Reflectivity, Principles and Applications*, Lecture Notes in Physics, Springer, Berlin (1999).
30. M. Tolan. *X-ray Scattering from Soft-Matter Thin Films*, Springer Tracts in Modern Physics, Springer, Berlin (1999).
31. V. Holy, U. Pietsch, T. Baumbach. *High Resolution X-ray Scattering from Thin Films and Multilayers*, Springer Tracts in Modern Physics, Springer, Berlin (1999).
32. J. Als-Nielsen and D. McMorrow. *Elements of Modern X-ray Physics*, Wiley, New York (2001).
33. A. Guinier and G. Fournet. *Small-Angle Scattering of X-Rays*, Wiley, New York (1955).
34. A. Gibaud, S. Hazra, C. Sella, P. Laffez, A. Désert, A. Naudon, G. Van Tendeloo. *Phys. Rev. B* **63**, 193407 (2001).
35. P. Moriarty. *Rep. Prog. Phys*. **64**, 297 (2001).
36. S. Kundu, S. Hazra, S. Banerjee, M. K. Sanyal, S. K. Mandal, S. Chaudhuri, A. K. Pal. *J. Phys. D* **31**, L73 (1998).
37. S. Hazra, S. Pal, S. Kundu, M. K. Sanyal. *App. Surf. Sci*. **182**, 244 (2001).
38. M. Milun, P. Pervan, D. P. Woodruff. *Rep. Prog. Phys*. **65**, 99 (2002).
39. H. H. Song, K. M. Jones, A. A. Baski. *J. Vac. Sci. Technol. A* **17**, 1696 (1999).
40. A. A. Baski, K. M. Saoud, K. M. Jones. *App. Surf. Sci*. **182**, 216 (2001).
41. B. K. Tanner, T. P. A. Hase, J. Clarke, I. Pape, A. Li-Bassi, B. D. Fulthorpe. *App. Surf. Sci*. **182**, 202 (2001).
42. M. K. Sanyal, S. Hazra, J. K. Basu, A. Datta. *Phys. Rev. B* **58**, R4258 (1998).
43. I. K. Robinson, I. A. Vartanyants, G. J. Williams, M. A. Pfeifer, J. A. Pitney. *Phys. Rev. Lett*. **87**, 195505 (2001).
44. M. K. Sanyal, J. K. Basu, A. Datta, S. Banerjee. *Europhys. Lett.* **36**, 265 (1996).
45. M. K. Sanyal, A. Datta, A. K. Srivatsava, B. M. Arora, S. Banerjee, P. Chakraborty, F. Caccavale, O. Sakata, H. Hashizume. *Appl. Surf. Sci.* **133**, 98 (1998).
46. A. Gibaud, N. Cowlam, G. Vignaud, T. Richardson. *Phys. Rev. Lett.* **74**, 3205 (1995).
47. J. Krug. *Adv. Phys.* **46**, 139 (1997).
48. M. K. Sanyal, S. K. Sinha, K. G. Huang, B. M. Ocko. *Phys. Rev. Lett.* **66**, 628 (1991).
49. A. Pimpinelli and J. Villain. *Physics of Crystal Growth*, Cambridge University Press, Cambridge (1998).
50. J. G. Amar, M. N. Popescu, F. Family. *Phys. Rev. Lett.* **86**, 3092 (2001).

51. A. L. Barabasi and H. E. Stanley. *Fractal Concepts in Surface Growth*, Cambridge University Press, New York (1995).
52. A. Malik, M. K. Durbin, A. G. Richter, K. G. Huang, P. Dutta. *Phys. Rev. B* **52**, R11654 (1995).
53. V. M. Kaganer, H. Möhwald, P. Dutta. *Rev. Mod. Phys.* **71**, 779 (1999).
54. A. Ulman. *Introduction to Ultrathin Organic Films*, Academic Press, New York (1991).
55. S. Mann. *Nature* **365**, 499 (1993).
56. I. Kuzmenko, H. Rapaport, K. Kjaer, J. Als-Nielsen, I. Weissbuch, M. Lahav, L. Leiserowitz. *Chem. Rev*. **101**, 1659 (2001).
57. J. M. Bloch and W. Yun. *Phys. Rev. A* **41**, 844 (1990).
58. J. Kmetko, A. Datta, G. Evmenenko, P. Dutta. *J. Phys. Chem. B* **105**, 10818 (2001).
59. F. Leveiller, C. Boehm, D. Jacquemain, H. Möhwald, L. Leiserowitz, K. Kjaer, J. Als-Nielsen. *Langmuir* **10**, 819 (1994).
60. J. Kmetko, A. Datta, G. Evmenenko, M. K. Durbin, A. G. Richter, P. Dutta. *Langmuir* **17**, 4697 (2001).
61. X. Peng, S. Guan, X. Chai, Y. Jiang, T. Li. *J. Phys. Chem. B* **96**, 3170 (1992).
62. L. S. Li, L. Qu, L. Wang, R. Lu, X. Peng, Y. Zhao, T. J. Li. *Langmuir* **13**, 6183 (1997).
63. S. Hazra, A. Gibaud, C. Sella. *J. Phys. D* **43**, 1575 (2001).
64. C. F. Chou, A. J. Jin, S. W. Hui, C. C. Huang, J. T. Ho. *Science* **280**, 1424 (1998).
65. R. Radhakrishnan. *Phys. Rev. Lett*. **89**, 076101 (2002).
66. W. J. Orts, J. H. Zanten, W. L. Wu, S. K. Satija. *Phys. Rev. Lett*. **71**, 867 (1993).